

A Learning Framework for Diffeomorphic Image Registration based on Quasi-conformal Geometry

Qiguang Chen*, Zhiwen Li*, and Lok Ming Lui*

Abstract. Image registration, the process of defining meaningful correspondences between images, is essential for a variety of image analysis tasks, especially medical imaging studies. Numerous learning-based methods, notably convolutional neural networks (CNNs), for deformable image registration proposed in recent years have demonstrated the feasibility and superiority of deep learning techniques for registration problem. Besides, compared to traditional algorithms' optimization scheme of the objective function for each image pair, learning-based algorithms are several orders of magnitude faster. However, these data-driven methods without proper constraint on the deformation field will easily lead to topology destruction, namely foldings. To tackle this problem, We propose the *quasi-conformal registration network* (QCRRegNet), a novel fast unsupervised learning framework, to obtain diffeomorphic 2D image registrations with large deformations based on quasi-conformal map, an orientation-preserving homeomorphism between two manifolds embedded in \mathbb{R}^2 . The basic idea is to design and train an end-to-end CNN which maps image pairs to the deformation fields. The proposed QCRRegNet consists of two parts, the *estimator network* and the *Beltrami solver network* (BSNet). The estimator network takes image pair as input and outputs the Beltrami coefficient, a complex-valued function with supreme norm strictly less than 1. The Beltrami coefficient, which captures all conformal distortion of a quasi-conformal map and guarantees the bijectivity, will then be input to the BSNet, a task-independent network which reconstructs the corresponding quasi-conformal map from its Beltrami coefficient, to obtain the desired deformation map. Furthermore, we reduce the number of network parameters and computational complexity by utilizing Fourier approximation to compress Beltrami coefficient. In this paper, experiments have been carried out on different data such as underwater and medical images. Registration results demonstrate that QCRRegNet's registration accuracy is comparable to state-of-the-art methods and diffeomorphism is to a great extent guaranteed compared to other diffeomorphic registration algorithms.

Key words. image registration, convolutional neural networks, quasi-conformal mapping, Beltrami coefficient, Beltrami solver network, quasi-conformal registration network

1. Introduction. Image registration is the process of finding the correspondence between images obtained from medical, industrial and other scenarios. It is widely used in medical image analysis, satellite data analysis, underwater image processing and etc. For instance, medical images captured at different time can reveal some information which can help improve diagnostic accuracy. Long distance photography usually incorporates atmospheric turbulence, which distorts the captured objects. Image registration can help analyze the distortion so as to be used to develop restoration methods. Tracking objects in different frames in a video is also a practical application of image registration in some industries.

Traditional registration methods usually align image pairs by solving optimization problems subjecting to certain constraints. However, iteratively solving optimization problems is computationally intensive, and takes a long time to approach the solution, varying from seconds to hundreds of seconds. Due to the lack of constraints on the output mapping, traditional registration methods tend to show foldings when the input images have complex details

*Department of Mathematics, The Chinese University of Hong Kong, Shatin, Hong Kong (im.ki@link.cuhk.edu.hk, zwli@math.cuhk.edu.hk, lmlui@math.cuhk.edu.hk).

and when the deformation is large.

Recently, deep neural networks show impressive performance in various image analysis tasks. Some attempts to apply neural network to image registration has been made. However, few of them takes the advantage of mathematical theory to enhance diffeomorphism of the mapping between image pairs.

In this paper, we propose a novel learning-based image registration method, QCRegNet, based on quasi-conformal geometry. The key idea is to obtain a task-independent Beltrami solver network (BSNet) which can convert Beltrami coefficient to its corresponding mapping, and an deformation estimator which can generate the Beltrami coefficient describing the deformation between image pairs. Both models are trained in unsupervised manners.

The contributions of our work are as follows:

- (i) We are the first to design a task-independent Beltrami Solver Network (BSNet) which can accurately generate approximated mappings given Beltrami coefficients. Fourier approximation of Beltrami Coefficient is introduced to reduce the computation while achieve good results.
- (ii) We propose a novel registration method based on Quasi-Conformal geometry, which enhances the diffeomorphism of the mapping. Compared with previous registration methods that require iterative optimization, our model is much faster since no iteration is required during the testing phase.

2. Related Works. For decades, numerous image registration algorithms have been proposed. Horn and Schunck [10] developed a method to find the optic flow pattern of sequences of images. Beg *et al.* [2] proposed the large deformation diffeomorphic metric mapping (LDDMM) for image warping. Joshi and Miller [12] proposed a method to generate large deformation diffeomorphisms for landmark matching. Image registration tools such as Elastix[13], deformable image registration using discrete optimization (DROP) [8] and flexible algorithms for image registration (FAIR) [16] were made available. The well-known hyperelastic regularization method [4] was later proposed to complement the FAIR framework.

Based on Thirion’s demons algorithm [20], Vercauteren *et al.*[21] developed the Diffeomorphic Demons (DDemons), an efficient algorithm for non-parametric diffeomorphic image registration. Inspired by DDemons and quasi-conformal theory, Lam and Lui proposed the Quasi-conformal hybrid registration (QCHR) [14] which successfully reduces the local geometric distortion of the registration map. QCHR was applied to solve various tasks, such as registration and shape analysis [5, 22], and achieve good results. However, these methods may not work well when landmarks are not accessible, and their iterative implementation takes a comparatively long time to approach the minimizer.

Recently, in order to avoid the time-consuming iterative optimization and find more accurate mappings, many efforts have been made to apply neural networks to image registration. Based on the Spatial Transformer Network (STN) [11], Bob D. de Vos *et al.*[6] proposed the Deep Learning Image Registration (DLIR) framework for unsupervised affine and deformable image registration. Balakrishnan *et al.*[1] proposed VoxelMorph, a learning-based framework for 2D or 3D image registration. VoxelMorph enforces the bijectivity by suppressing the norm of the velocity vector field so as to meet the assumption mentioned in [2]. However, simply constraining the norm of the velocity vector field is still too rough to ensure the diffeomorphism

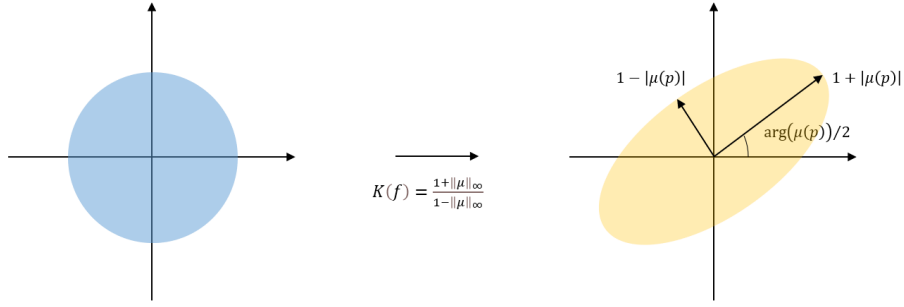


Figure 1: Illustration of how the Beltrami coefficient determines the conformal distortion of a quasi-conformal map.

of the corresponding mapping.

3. Background.

3.1. Quasi-Conformal mapping and Beltrami Coefficient. As a generalization of conformal maps, the angle-preserving homeomorphisms between Riemann surfaces, quasi-conformal maps, orientation-preserving homeomorphisms between Riemann surfaces with bounded conformality distortion, are a suitable class of diffeomorphisms for studying image/surface registration. Mathematically, $f : \mathbb{C} \rightarrow \mathbb{C}$ is *quasi-conformal* provided that it satisfies the Beltrami equation

$$(3.1) \quad \frac{\partial f}{\partial \bar{z}} = \mu(z) \frac{\partial f}{\partial z}$$

for some complex-valued Lebesgue measurable function μ satisfying $\|\mu\|_\infty < 1$. μ is called the *Beltrami Coefficient* of f . The *Beltrami Coefficient* μ , a measure of nonconformality, measures how far the map at each point is deviated from a conformal map. In particular, the map f is conformal around a small neighborhood of p when $\mu_p = 0$. Infinitesimally, around a point p , f may be expressed with respect to its local parameter as follows:

$$(3.2) \quad f(z) \approx f(p) + f_z(p)z + f_{\bar{z}}(p)\bar{z} = f(p) + f_z(p)(z + \mu(p)\bar{z})$$

Obviously, f is not conformal if and only if $\mu(p) \neq 0$. Inside the local parameter domain, f may be considered as a map composed of a translation to $f(p)$ together with a stretch map $S(z) = z + \mu(p)\bar{z}$, which is postcomposed by a multiplication of $f_z(p)$, which is conformal. All the conformal distortion of $S(z)$ is caused by $\mu(p)$. $S(z)$ is the map that causes f to map a small circle to a small ellipse. From $\mu(p)$, we can determine the angles of the directions of maximal magnification and shrinking and the amount of them as well. Specifically, the angle of maximal magnification is $\arg(\mu(p))/2$ with magnifying factor $1 + |\mu(p)|$; the angle of maximal shrinking is the orthogonal angle $(\arg(\mu(p)) - \pi)/2$ with shrinking factor $1 - |\mu(p)|$. Thus, the BC μ gives us all the information about the conformality of f (see [Figure 1](#)).

Given a Beltrami coefficient $\mu : \mathbb{C} \rightarrow \mathbb{C}$ with $\|\mu\|_\infty < 1$, there is always a quasi-conformal mapping from \mathbb{C} onto itself which satisfies the Beltrami equation in the distribution sense [7]. More precisely, we have the following.

Theorem 3.1. *Suppose $\mu : \mathbb{D} \rightarrow \mathbb{C}$ is Lebesgue measurable satisfying $\|\mu\|_\infty < 1$; then there is a quasi-conformal homeomorphism ϕ from the unit disk to itself, which is in the Sobolev space $W^{1,2}(\Omega)$ and satisfies the Beltrami equation (3.1) in the distribution sense. Furthermore, by fixing 0 and 1, the associated quasi-conformal homeomorphism ϕ is uniquely determined.*

Given an orientation preserving homeomorphism ϕ , we can find the corresponding BCs from the Beltrami equation:

$$(3.3) \quad \mu_\phi = \frac{\partial\phi}{\partial\bar{z}} / \frac{\partial\phi}{\partial z}$$

The Jacobian J of ϕ is related to μ_ϕ as follows:

$$(3.4) \quad J(\phi) = \left| \frac{\partial\phi}{\partial z} \right|^2 (1 - |\mu_\phi|^2)$$

Since ϕ is an orientation preserving homeomorphism, $J(\phi) > 0$ and $|\mu_\phi| < 1$ everywhere. Hence, we must have $\|\mu_\phi\|_\infty < 1$. Furthermore, Theorem 3.1 suggest that under suitable normalization, every μ with $\|\mu\|_\infty < 1$ is associated with a unique homeomorphism. We can therefore conclude that there is a 1-1 correspondence between the set of all quasiconformal homeomorphisms and the set of all BCs with supreme norm less than 1. In other words, a homeomorphism from \mathbb{C} or \mathbb{D} onto itself can be uniquely determined by its associated BC.

3.2. Linear Beltrami Solver. [15] proposed an efficient algorithm to reconstruct the associated quasi-conformal homeomorphism when given a Beltrami representation.

Suppose M_1 and M_2 are two images. Given a Beltrami representation μ on M_1 , our goal is to reconstruct the associated homeomorphism $f : M_1 \rightarrow M_2$ between M_1 and M_2 .

Let $f = u + iv$, where $i = \sqrt{-1}$. From the Beltrami equation (3.1), we have

$$(3.5) \quad \mu(f) = \frac{(u_x - v_y) + i(v_x + u_y)}{(u_x + v_y) + i(v_x - u_y)}$$

Let $\mu(f) = \rho + i\tau$. We can write v_x and v_y as linear combinations of u_x and u_y ,

$$(3.6) \quad \begin{aligned} -v_y &= \alpha_1 u_x + \alpha_2 u_y \\ v_x &= \alpha_2 u_x + \alpha_3 u_y \end{aligned}$$

where $\alpha_1 = \frac{(\rho-1)^2 + \tau^2}{1-\rho^2-\tau^2}$; $\alpha_2 = -\frac{2\tau}{1-\rho^2-\tau^2}$; $\alpha_3 = \frac{(\rho+1)^2 + \tau^2}{1-\rho^2-\tau^2}$. Similarly,

$$(3.7) \quad \begin{aligned} -u_y &= \alpha_1 v_x + \alpha_2 v_y \\ u_x &= \alpha_2 v_x + \alpha_3 v_y \end{aligned}$$

Since $\nabla \cdot \begin{pmatrix} -v_y \\ v_x \end{pmatrix} = 0$, we obtain

$$(3.8) \quad \nabla \cdot \left(A \begin{pmatrix} u_x \\ u_y \end{pmatrix} \right) = 0 \text{ and } \nabla \cdot \left(A \begin{pmatrix} v_x \\ v_y \end{pmatrix} \right) = 0, \quad A = \begin{pmatrix} \alpha_1 & \alpha_2 \\ \alpha_2 & \alpha_3 \end{pmatrix}$$

Besides, f has to satisfy certain constraints on the boundary. For example, when M_1 is a topological disk, the parameter domain D is a unit square. In this case, the desired quasi-conformal map should satisfy

$$(3.9) \quad \begin{aligned} f(0) &= 0; & f(1) &= 1; & f(i) &= i; & f(1+i) &= 1+i; \\ \operatorname{Re}(f) &= 0 \text{ on arc } [0, i]; & \operatorname{Re}(f) &= 1 \text{ on arc } [1, 1+i]; \\ \operatorname{Im}(f) &= 0 \text{ on arc } [0, 1]; & \operatorname{Im}(f) &= 1 \text{ on arc } [i, 1+i]; \end{aligned}$$

3.3. Numerical Implementation of LBS. Given the Beltrami Coefficient μ , we can reconstruct the corresponding quasi-conformal mapping f by solving (3.8)

In discrete case, the parameter domain D is a mesh grid. The restriction of f on each triangular face T is linear and can be written as

$$(3.10) \quad f|_T(x, y) = \begin{bmatrix} u|_T(x, y) \\ v|_T(x, y) \end{bmatrix} = \begin{bmatrix} a_T x + b_T y + r_T \\ c_T x + d_T y + s_T \end{bmatrix}$$

Obviously, on each face, we have induced partial derivatives from the face-wise linear assumption.

Hence, the partial derivatives of f at each face T can be denoted as $D_x f(T) = a_T + ic_T$ and $D_y f(T) = b_T + id_T$. Now the gradient $\nabla_T f := (D_x f(T), D_y f(T))^t$ on T can be computed by solving

$$(3.11) \quad \begin{pmatrix} v_1 - v_0 \\ v_2 - v_0 \end{pmatrix} \nabla_T f_i = \begin{pmatrix} f_i(\vec{v}_1) - f_i(\vec{v}_0) \\ f_i(\vec{v}_2) - f_i(\vec{v}_0) \end{pmatrix}$$

where $[\vec{v}_0, \vec{v}_1]$ and $[\vec{v}_0, \vec{v}_2]$ are two edges on T .

Besides, μ is a face-based function. Denote the face-based function α_i on face T by α_i^T , where $i = 1, 2, 3$. From (3.6) and (3.7), we have

$$(3.12) \quad \begin{aligned} -d_T &= \alpha_1^T a_T + \alpha_2^T b_T \\ c_T &= \alpha_2^T a_T + \alpha_3^T b_T \end{aligned}$$

and

$$(3.13) \quad \begin{aligned} -b_T &= \alpha_1^T c_T + \alpha_2^T d_T \\ a_T &= \alpha_2^T c_T + \alpha_3^T d_T \end{aligned}$$

Let $T = [\vec{v}_i, \vec{v}_j, \vec{v}_k]$ and $w_I = f(\vec{v}_I)$, where $I = i, j, k$. Suppose $v_I = g_I + ih_I$ and $w_I = s_I + it_I$ ($I = i, j, k$). Using (3.11), According to mapping (3.11), for each face T , we have

$$(3.14) \quad \begin{bmatrix} a_T & b_T \\ c_T & d_T \end{bmatrix} \begin{bmatrix} g_j - g_i & g_k - g_i \\ h_j - h_i & h_k - h_i \end{bmatrix} = \begin{bmatrix} s_j - s_i & s_k - s_i \\ t_j - t_i & t_k - t_i \end{bmatrix}$$

Thus,

$$(3.15) \quad \begin{bmatrix} a_T & b_T \\ c_T & d_T \end{bmatrix} = \frac{1}{2 \cdot \text{Area}(T)} \begin{bmatrix} s_j - s_i & s_k - s_i \\ t_j - t_i & t_k - t_i \end{bmatrix} \begin{bmatrix} h_k - h_i & g_i - g_k \\ h_i - h_j & g_j - g_i \end{bmatrix}$$

$$(3.16) \quad = \begin{bmatrix} A_i^T s_i + A_j^T s_j + A_k^T s_k & B_i^T s_i + B_j^T s_j + B_k^T s_k \\ A_i^T t_i + A_j^T t_j + A_k^T t_k & B_i^T t_i + B_j^T t_j + B_k^T t_k \end{bmatrix}$$

where

$$(3.17) \quad \begin{aligned} A_i^T &= (h_j - h_k) / 2 \cdot \text{Area}(T); & B_i^T &= (g_k - g_j) / 2 \cdot \text{Area}(T) \\ A_j^T &= (h_k - h_i) / 2 \cdot \text{Area}(T); & B_j^T &= (g_i - g_k) / 2 \cdot \text{Area}(T) \\ A_k^T &= (h_i - h_j) / 2 \cdot \text{Area}(T); & B_k^T &= (g_j - g_i) / 2 \cdot \text{Area}(T) \end{aligned}$$

For each vertex v_i , let N_i be the collection of neighborhood faces attached to v_i . By careful checking, one can observe that

$$(3.18) \quad \sum_{T \in N_i} A_i^T b_T = \sum_{T \in N_i} B_i^T a_T; \quad \sum_{T \in N_i} A_i^T d_T = \sum_{T \in N_i} B_i^T c_T;$$

Substituting Equations (3.12) and (3.13) into (3.18), we obtain the following equations

$$(3.19) \quad \sum_{T \in N_i} (A_i^T [\alpha_1^T a_T + \alpha_2^T b_T] + B_i^T [\alpha_2^T a_T + \alpha_3^T b_T]) = 0$$

$$(3.20) \quad \sum_{T \in N_i} (A_i^T [\alpha_1^T c_T + \alpha_2^T d_T] + B_i^T [\alpha_2^T c_T + \alpha_3^T d_T]) = 0$$

Replacing a_T , b_T , c_T and d_T with their corresponding expressions, we derive the following coefficient for the central vertex i of N_i

$$(3.21) \quad c_i = \sum_{T \in N_i} [\alpha_1^T (A_i^T)^2 + 2\alpha_2^T A_i^T B_i^T + \alpha_3^T (B_i^T)^2]$$

For two incident triangular faces $T_1, T_2 \in N_i$, the edge e between T_1 and T_2 connect the central vertex i and another vertex v , as shown in Figure 2. In this case, the index of vertex v in T_1 is j , and that in T_2 is k . The coefficient of vertex v can then be written as follow

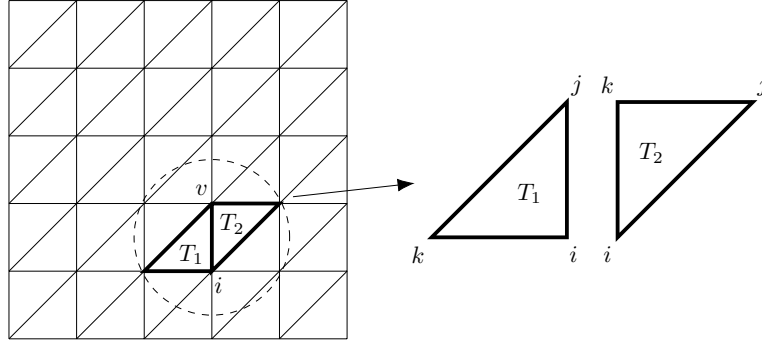


Figure 2: Illustration of the derivation of the coefficient of vertex v

$$(3.22) \quad c_v = \alpha_1^{T_1} A_i^{T_1} A_j^{T_1} A_k^{T_1} + \alpha_2^{T_1} (A_i^{T_1} B_j^{T_1} + A_j^{T_1} B_i^{T_1}) + \alpha_3^{T_1} B_i^{T_1} B_j^{T_1} B_k^{T_1} + \alpha_1^{T_2} A_i^{T_2} A_k^{T_2} A_j^{T_2} + \alpha_2^{T_2} (A_i^{T_2} B_k^{T_2} + A_k^{T_2} B_i^{T_2}) + \alpha_3^{T_2} B_i^{T_2} B_k^{T_2} B_j^{T_2}$$

According to Equation (3.21), (3.22), (3.19) and (3.20), for a vertex i , we can write down the following equations

$$(3.23) \quad \begin{aligned} c_i s_i + \sum_{v \in V_i} c_v s_v &= 0 \\ c_i t_i + \sum_{v \in V_i} c_v t_v &= 0 \end{aligned}$$

where V_i is the set of adjacent vertices of vertex i .

For an $N \times N$ mesh grid, we have

$$(3.24) \quad \begin{aligned} C_s \mathbf{s} &= \mathbf{0} \\ C_t \mathbf{t} &= \mathbf{0} \end{aligned}$$

where \mathbf{s} and \mathbf{t} are the $N \times N$ dimensional coordinate vectors, in which the entries of boundary constraints set to their true values. C_s and C_t are the same $N^2 \times N^2$ sparse matrix, each row of which contains c_i and c_v for a vertex in the mesh grid. The only difference between C_s and C_t is that the rows that correspond to the boundary constraints of the two coordinates are set to 0.

Solving this linear system with the boundary constraints, we can obtain the corresponding mapping f given a Beltrami coefficient μ_f .

3.4. Convolutional Neural Networks (CNNs). Convolutional Neural Networks are a class of neural networks that are dedicated to visual tasks. In the recent decade, CNNs have achieved state-of-the-art performance in various visual tasks such as image classification, segmentation, super-resolution and etc.

CNNs generally consist of a variety of layers such as convolution layer and pooling layer. Convolution layers include convolution kernels that slide through images and perform local multiplication and summation. These kernels are learned by optimizing certain loss functions

given some datasets. To introduce non-linearity, a convolution operation is usually followed by an activation function such as Sigmoid or ReLU function. Other operations such as pooling or batch normalization can also be inserted between them to do down sampling or reduce internal covariate shift.

By stacking convolution layers, deeper layers can combine pattern from layers before them to generate more complex pattern, which make it possible to handle complicate tasks and achieve great results. In this paper, we use CNNs to estimate Beltrami coefficients that describe the distortion between source and target images, and generate the corresponding mapping. One can find details of CNN in [9].

3.5. Fourier Approximation for Beltrami Representation. [15] shows that Fourier approximation for Beltrami representation can easily preserve the mapping information while that for the representation of coordinate functions fails to enforce the homeomorphism. Comparing with the latter method which requires that the Jacobian of the coordinate functions has to be greater than 0, Fourier approximation for Beltrami representation requires only that the supreme norm must be less than 1, which is easier to be satisfied.

In the discrete case, an $N \times N$ Beltrami coefficient μ can be separated into two images representing the real and imaginary parts, μ_r and μ_i , respectively. The DFT of μ_r is

$$(3.25) \quad \hat{\mu}_r(m, n) = \frac{1}{N^2} \sum_{k=0}^{N-1} \sum_{l=0}^{N-1} \mu_r(k, l) e^{-\sqrt{-1} \frac{2\pi km}{N}} e^{-\sqrt{-1} \frac{2\pi ln}{N}}$$

This is equivalent to

$$(3.26) \quad \hat{\mu}_r = U \mu_r U$$

where $U_{kl} = \frac{1}{N} e^{-\sqrt{-1} \frac{2\pi kl}{N}}$, $0 \leq k, l \leq N-1$. The inverse DFT of $\hat{\mu}_r$ is

$$(3.27) \quad \mu_r(p, q) = \sum_{m=0}^{N-1} \sum_{n=0}^{N-1} \hat{\mu}_r(m, n) e^{\sqrt{-1} \frac{2\pi pm}{N}} e^{\sqrt{-1} \frac{2\pi qn}{N}}$$

which can be rewritten as

$$(3.28) \quad \mu_r = (NU^*) \hat{\mu}_r (NU^*)$$

When using Fourier coefficients $\hat{\mu}_r, \hat{\mu}_i$ to approximate Beltrami coefficients, we keep only a small fraction of the frequency components which acts as the low frequency components. This is equivalent to say that only a small fraction of the frequency components can well capture the majority of deformation. Motivated by this idea, we propose the Beltrami Solver Network (BSNet) which takes a Beltrami coefficient as input and use the Fourier approximation to represent the global information of the input.

4. Proposed Method. In this section, we describe in detail our proposed method for image registration. Given a source image I_s and a target image I_t , our goal is to design a model $\phi(I_s, I_t)$ to output the mapping from I_s to I_t . ϕ includes two parts, an estimator network (Estimator) which takes two images as its input and generates the Beltrami coefficient μ representing the distortion between the two images and a Beltrami Solver Network (BSNet) which converts the Beltrami coefficients μ to its corresponding mapping f .

Since the Estimator relies on the BSNet, BSNet should be trained before the Estimator. After sampling from the source image according to the output mapping $f = \phi(I_s, I_t)$, the registered image can be retrieved.

The model framework is summarized in Figure 3. The following sections introduce the details of BSNet and Estimator and the loss functions used to optimize the model.

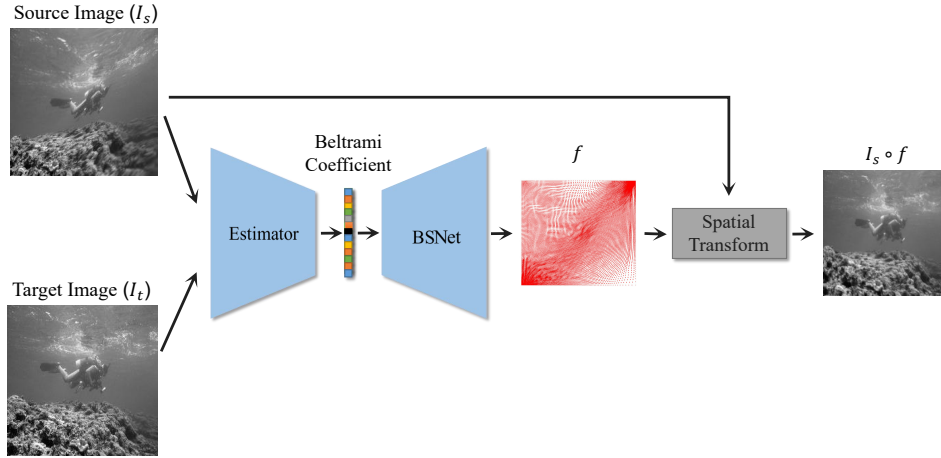


Figure 3: The architecture of the proposed Quasi-conformal Registration Network (QCRegNet).

4.1. Beltrami Solver Network. To make the idea feasible, the first component required is a network to convert Beltrami coefficients to their corresponding mappings. In the previous work [15], the conversion from Beltrami coefficients to mappings is achieved by using Linear Beltrami Solver (LBS), in which a sparse linear system is required to be solved. In this paper, we are going to use a neural network to approximate the mappings given their corresponding Beltrami Coefficients. There are two benefits. On the one hand, once trained, a well-designed neural network gives predictions much faster than solving the sparse linear system. On the other hand, neural network can back propagate errors from its output to input, which makes it possible to use a trained neural network as a component when training another network to solve a complicated task.

From above we notice that a single Beltrami coefficient μ_{ij} represents the distortion of a local region, where i and j represent the indices of a triangle in the spatial position. The global distortion depends on the entire Beltrami coefficient μ , since the mapping is obtained by solving the linear system. It is natural that we can use cascaded convolutional and down-

sampling layers to extract global information from the Beltrami coefficients, which can then be used to predict the mappings. The network structure should be similar to U-Net[18].

However, we learn the prior knowledge from [15] that Beltrami representation can be easily compressed by Fourier approximation, which means that low frequency components hold most of the global distortion information. With this prior knowledge, we can further simplify the network structure. Compared with convolutional layer, Fourier Transform has no trainable parameter and is much faster. And the generated low frequency component has only two channels, much less than the deep features extracted by neural networks. As a result, we use Fourier Transform to extract global information.

Once we use the Fourier approximation, we have to think about how to combine spatial operations, such as convolution and interpolation, and the Fourier coefficients on the frequency domain. Directly performing such operations on the frequency domain easily lead to poor performance. It is critical to introduce a layer for transforming the frequency features to the spatial domain.

Considering that the size of the deep spatial features or Fourier coefficient mentioned above is different from the input images and the Beltrami coefficient, we cannot use (3.26) and (3.28) directly.

In order to tackle this problem, we propose the Domain Transform Layer (DTL) which imitate the computation of (3.26) and (3.28). This layer can be formulated

$$(4.1) \quad \begin{aligned} \hat{\mu} &= M\mu N = (\mu^T M^T)^T N \\ \mu &= M\hat{\mu} N = (\hat{\mu}^T M^T)^T N \end{aligned}$$

where M and N are trainable complex matrix. This layer can be implemented by stacking two 1×1 convolution layers, together with some permutation operations.

As shown in subsection 4.1, given an input feature map of shape (H, W, C) , we can permute the feature map to be (H, C, W) . Then we perform K kernels 1×1 convolution. The shape of the resulting feature map should be (H, C, K) . These operations are equivalent to matrix multiplication of a $H \times W$ matrix and a $W \times K$ matrix.

From (4.1) we notice that (4.1) can be implemented by stacking two matrix multiplication blocks. The detail structure is shown in Figure 4. In our experiments, $H = W = K = L = 14$.

With DTL, the features in spatial domain can be transformed to a proper domain where spatial operations work. We can then perform convolution and upsampling on the features to obtain the mappings.

However, during the experiments, we found that the output mappings of the network are quite similar with their ground truth. But the outputs of the network have less details. In order to remedy this problem, we introduce a second path to improve the local details of the distortion, which are discarded in the computation of approximated Beltrami representation in the first path.

As in Figure 6, the second path is the upper path. In this skip path, a convolution and a down sampling are performed on the input μ , after which two more convolution layers are performed and the output features are concatenated to the output from the first path. Experimental results in the following sections show the necessity of this skip path.

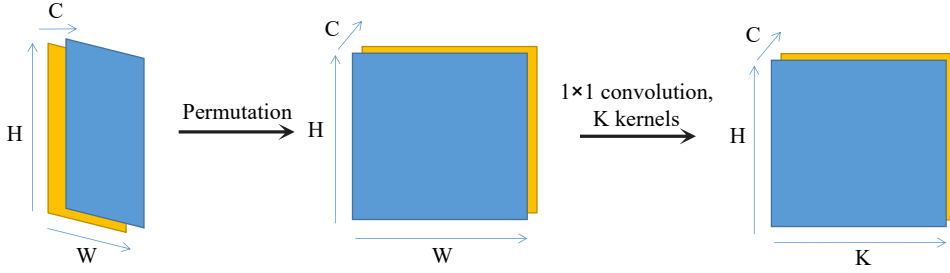


Figure 4: Matrix multiplication in the domain transform layer

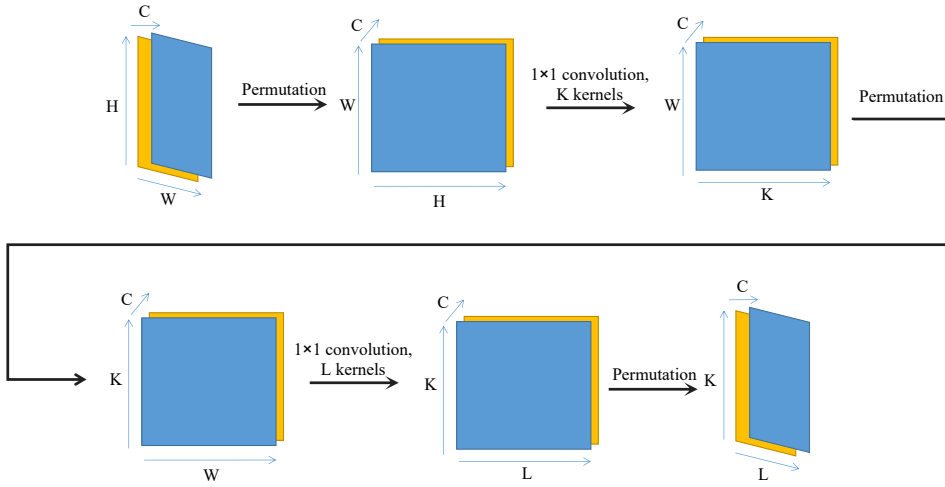


Figure 5: Domain Transform Layer

We trained this network in an unsupervised setting. As mentioned in [subsection 3.2](#), a single value in the Beltrami coefficient represents the distortion of a triangular face. The shape of the Beltrami coefficient describing an $N \times N$ image should be $(N - 1) \times [2 \times (N - 1)]$. Due to this reason, LBS takes an $(N - 1) \times 2 \times (N - 1)$ dimensional vector as its input. However, in this paper, we wish to ensure the consistency between the input and output of our model. To cope with this conflict, we adopt the following method.

Countless $N \times N$ Beltrami coefficients μ_{sqr} are generated by stacking pairs of images in the ILSVRC2012 dataset, which are augmented with some data augmentation tricks, such as random crop and flipping. μ_{sqr} serves as the input of BSNet, representing the Beltrami coefficients of the triangles with odd indices in each row. An $(N - 1) \times [2 \times (N - 1)]$ Beltrami coefficient μ_{rect} is then obtained by removing the last row and column of μ_{sqr} and interpolating the Beltrami coefficients representing the triangles with even indices with the values representing the surrounding faces. the linear system in the LBS can then be retrieved with μ_{rect} , the coefficients of which are then used to compute the loss.

In Quasi-conformal geometry, every vertex with index i in a mesh satisfies Equations

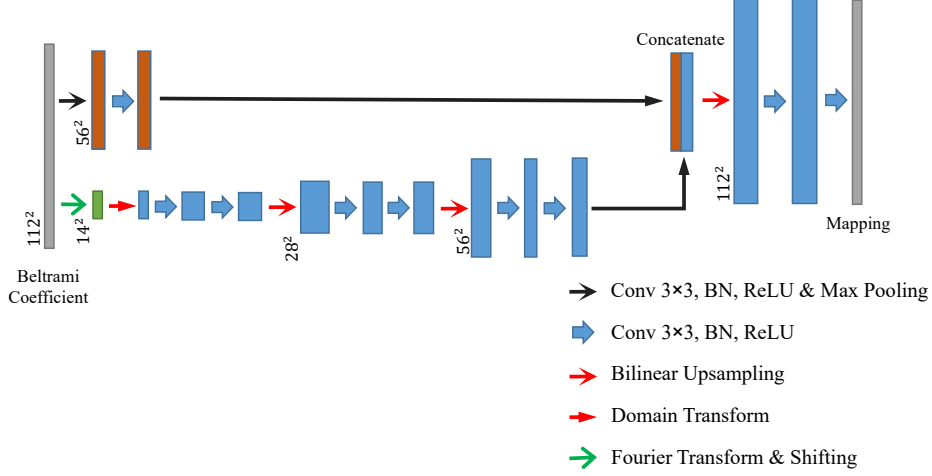


Figure 6: The architecture of the Beltrami Solver Network (BSNet).

(3.24). It is natural to regard Equations (3.24) as a loss function when training neural network to approximate the ground truth mapping of a given Beltrami coefficient μ .

The loss function can be formulated as follow

$$(4.2) \quad L_{Lapla} = \frac{1}{2N^2} (\|C_s \mathbf{s}\|_1 + \|C_t \mathbf{t}\|_1)$$

$$(4.3) \quad L_{BSNet} = \gamma L_{Lapla}$$

Note that each row in C_s and C_t represents the relationship between a certain pixel and the pixels adjacent to it. In the context of triangular mesh, a pixel is adjacent to at most six pixels. So each row in C_s and C_t has at most seven nonzero elements. Although the two $N^2 \times N^2$ matrices C_s and C_t are sparse, both matrices can be rewritten as two dense arrays in the implementation of our method, which means that the computation of L_{BSNet} is memory saving and efficient.

4.2. Estimator. Another component in the proposed algorithm is the Estimator Network which takes the source and target images as its input and generates the corresponding Beltrami coefficient representing the distortion of the input images. The network is based on U-Net[18] with an activation added to its output. Its framework is shown in Figure 7.

Estimator performs convolution and pooling to extract the deep spatial features of the two input images. These deep spatial features are then up-sampled to be a two channel image $\tilde{\mu}$ from which the norm and angle of $\tilde{\mu}$ can be computed. Notice that when we train Estimator, we assume that a BSNet has been trained so that for any μ satisfies $\|\mu\|_2 < 1$, it can convert the μ to its corresponding mapping. Naturally, μ generated by Estimator should also satisfy

this condition. In order to ensure $\|\mu\|_2 < 1$, we add a *Tanh* activation which takes $\tilde{\mu}$ as its input.

$$\|\mu\|_2 = \text{Tanh}(\|\tilde{\mu}\|_2)$$

where

$$\text{Tanh}(x) = \frac{e^x - e^{-x}}{e^x + e^{-x}}$$

Since $\|\tilde{\mu}\|_2 \geq 0$, $1 > \|\mu\|_2 \geq 0$ always holds. Then we have

$$(4.4) \quad \begin{aligned} \text{Re}(\mu) &= \|\mu\|_2 \cos(\text{Arg}(\tilde{\mu})) \\ \text{Im}(\mu) &= \|\mu\|_2 \sin(\text{Arg}(\tilde{\mu})) \end{aligned}$$

μ serves as the Beltrami coefficient representing the deformation between the two input images.

We also use the following loss function to suppress the norm of μ

$$(4.5) \quad L_\mu = \frac{1}{N} \sum_{n=1}^N \|\mu\|_2^2.$$

The smoothness can be enhanced by

$$(4.6) \quad L_{smooth} = \frac{1}{N} \sum_{n=1}^N \|\nabla \mu\|_2^2.$$

The fidelity term is as follow

$$(4.7) \quad L_F = \frac{1}{N} \sum_{n=1}^N \|I_s \circ f - I_t\|_2^2.$$

The total loss function is

$$(4.8) \quad L_{Estimator} = \alpha L_F + \beta L_\mu + \eta L_{smooth}$$

where α , β , and η are hyper-parameters that give different weighting to the corresponding terms.

5. Evaluation. In this paper, we use two indicators to demonstrate the superiority of our proposed model.

- The number of triangular faces where $|J| \leq 0$. As mentioned in [subsection 3.2](#), images are separated into triangular faces in which linear operation is performed. On each triangular face, we calculate the determinant of its Jacobian matrix $|J| \leq 0$. $|J| \leq 0$ means folding occurs in the corresponding triangular face. This indicator shows the number of folded triangular faces.
- The sum of the absolute value of $|J|$ less than or equal to 0. We use this indicator to show the extent of the folding. As shown in [subsection 7.3](#), the larger this indicator is, the worse the performance is.

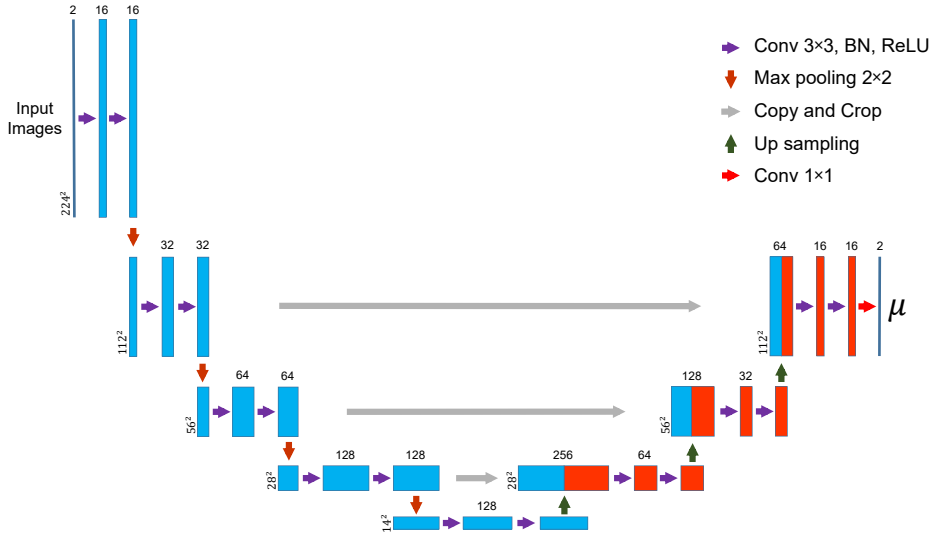


Figure 7: The architecture of the Estimator Network.

6. Implementation.

6.1. Training Schemes. The experiments are conducted in PyTorch [17] with a CUDA-enabled GPU. In our experiments, we first train the BSNet, and then use the trained BSNet to guide the training process of Estimator by converting the Beltrami coefficient μ to its corresponding mapping, which is subsequently used to compute the loss function.

We use the RMSprop optimizer with a momentum of 0.9 to train the two models. When training the BSNet, the learning rate is set to 0.0002, γ is set to 50. We set the hyper-parameters of Estimator, α , β and η to 400, 1 and 1 correspondingly. The learning rate is 0.00002. Both models are trained for 2000 epochs.

Since the function of BSNet is to convert any given Beltrami coefficients to their corresponding deformations, this network is irrelevant to the specific tasks. So there is no need to retrain BSNet when we face a new task with the same input shape.

Although we train BSNet in an unsupervised method, we need to synthesize sufficient Beltrami coefficients to train it. The dataset used to synthesize Beltrami coefficients is ILSVRC2012 [19], which has sufficient images to support the training.

To demonstrate the efficiency of our proposed algorithm, for each real world image registration task, we also trained a VoxelMorph model with the same dataset and preprocessing methods and its default hyper-parameters for 2000 epochs. The experimental results show the superiority of our proposed model.

7. Experiment Results. In this paper, we are going to apply our proposed QCRegNet to some real world image registration scenarios such as underwater image registration and medical image registration. Since the performance of our model inevitably relies on the efficacy of BSNet, we must first ensure that BSNet is properly designed. In the following subsections,

we will first show some results to support the efficacy of BSNet, after which the results in some real world scenarios will be shown.

7.1. BSNet without Domain Transform Layer. In [subsection 7.1](#) and [Figure 8](#), mapping (a) is generated by LBS; (b) is generated by our proposed BSNet; (c) is generated by BSNet that has the Domain Transform Layer removed, which is denoted as BSNet-noDTL; (d) and (e) are generated by modified BSNet, in which the Domain Transform Layer is replaced by 1 and 2 convolutional layers respectively, which are denoted as BSNet-conv1 and BSNet-conv2. The convolutional layers used in (d) and (e) have 64 kernels. All the models were trained with the same hyper-parameters for 2000 epochs.

From (b) in [subsection 7.1](#) and [Figure 8](#), we notice that BSNet can generate a mapping similar to that generated by LBS. The resulting mappings (c) indicate that a BSNet without DTL fails to convert Beltrami coefficients to their corresponding mappings. (d) and (e) show that although convolutional layers have the ability to convert information from the frequency domain to the spatial domain, this ability is weaker than that of DTL.

Numerically, we compared L_{Lapla} of the four models on a 10000 Beltrami coefficients dataset. L_{Lapla} of BSNet is 0.000291, which is the lowest loss. BSNet-conv2 got 0.000395, which means that DTL performs better in converting information from the frequency domain to the spatial domain when compared with 2 convolutional layers. After removing a convolutional layer, the loss of this model increased to 0.000470. The BSNet-noDTL got the highest loss, which is 0.000654. These experimental results show the superiority of the Domain Transform Layer.

7.2. Necessity of the Two Paths in BSNet. In this section, we refer to the upper path in [Figure 6](#), including down-sampling, convolution and concatenation operations, as the short path. The other path that has the Domain Transform Layer and up-sampling operations is referred to as the long path.

In [subsection 7.2](#) and [Figure 10](#), (a) is the target mapping generated by LBS; (b) is the result of our BSNet; (c) is the result of LBS with a Fourier approximation of the Beltrami coefficient as the input of LBS; (d) and (e) are the results of the modified BSNet without the short and long path respectively.

Comparing (b) and (d), we notice that (b) has more details than (d), which indicates that the short path in BSNet can provide more local information of the distortion. It makes sense because a single value of a given Beltrami coefficient represents the deformation of a certain triangular face in the mesh. (b) and (e) show that the short path cannot provide enough global information of the deformation to support the conversion. (c) has more details than (d), which means that the long path cannot completely preserve the details hidden inside the Fourier coefficient. The comparison shows that both the short and long paths are necessary in generating the target mapping of a given Beltrami coefficient.

We also compared L_{Lapla} of the three models on the same Beltrami coefficients dataset used in [subsection 7.1](#). L_{Lapla} of BSNet without the short path is 0.000528, which is higher than that of BSNet (0.000291). The model with only the short path got 0.004119, which means that the model is unable to generate the correct mappings of the given Beltrami coefficients. The experimental results show the necessity of the two paths in BSNet.

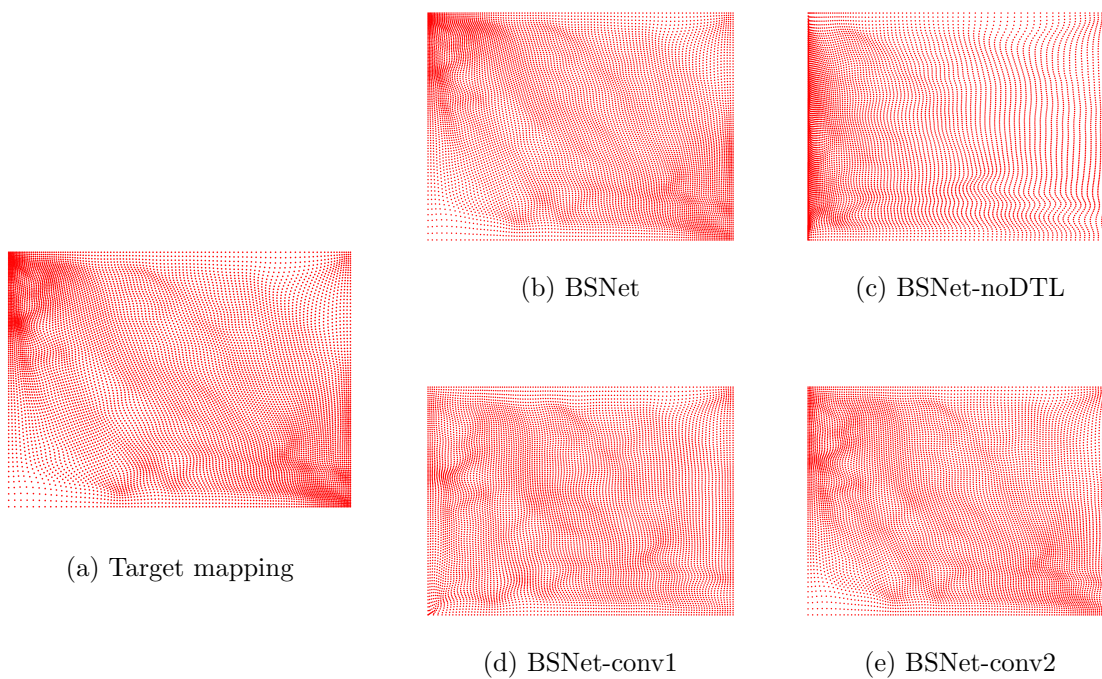


Figure 8: Examples generated by experiment of replacing DTL with different structure.

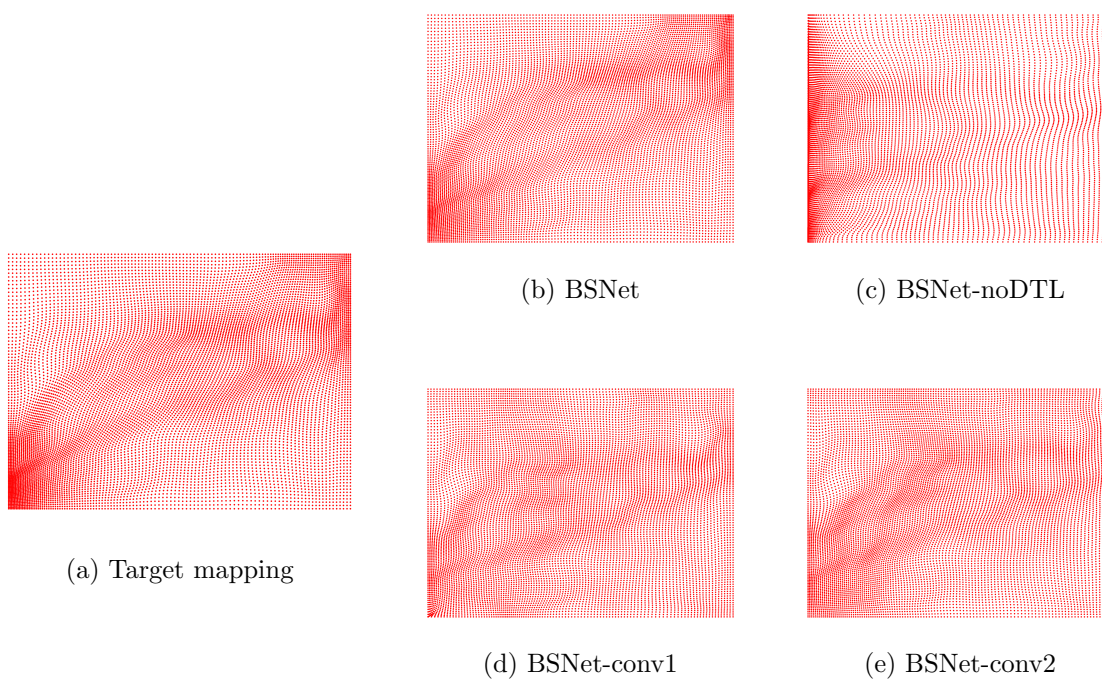


Figure 9: Examples generated by experiment of replacing DTL with different structure.

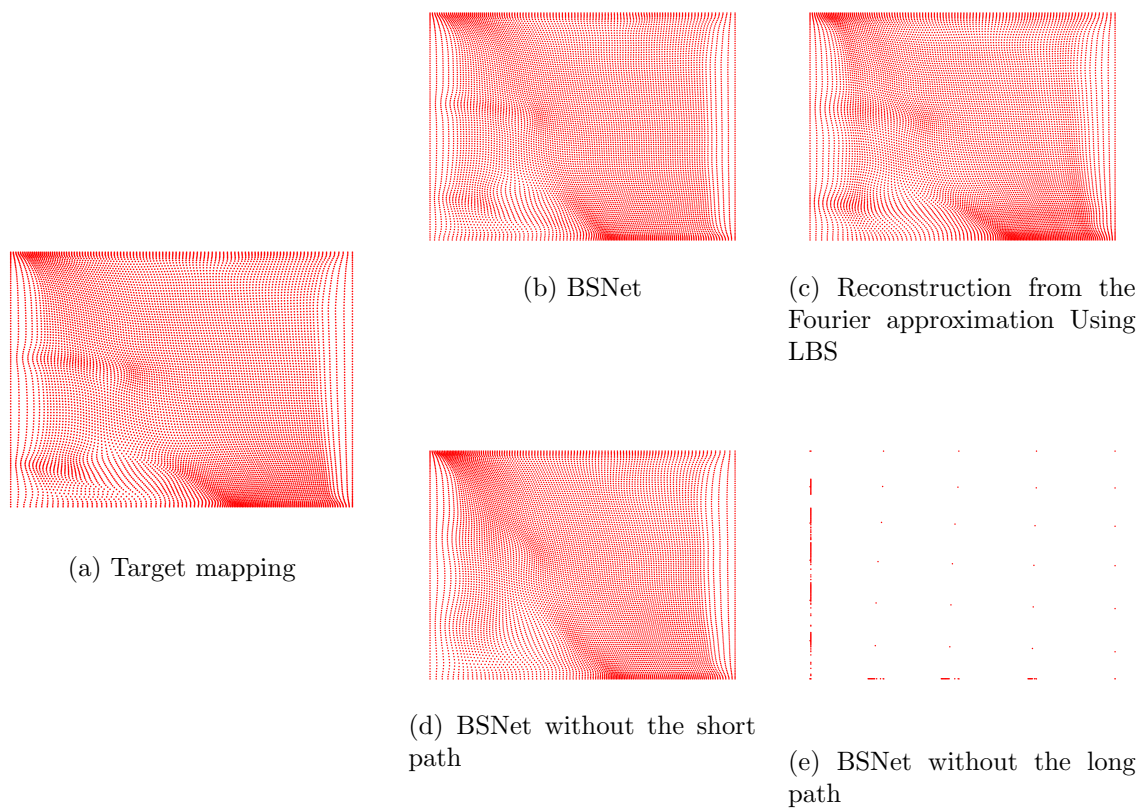


Figure 10: Examples generated by experiment of removing the short path or the long path.

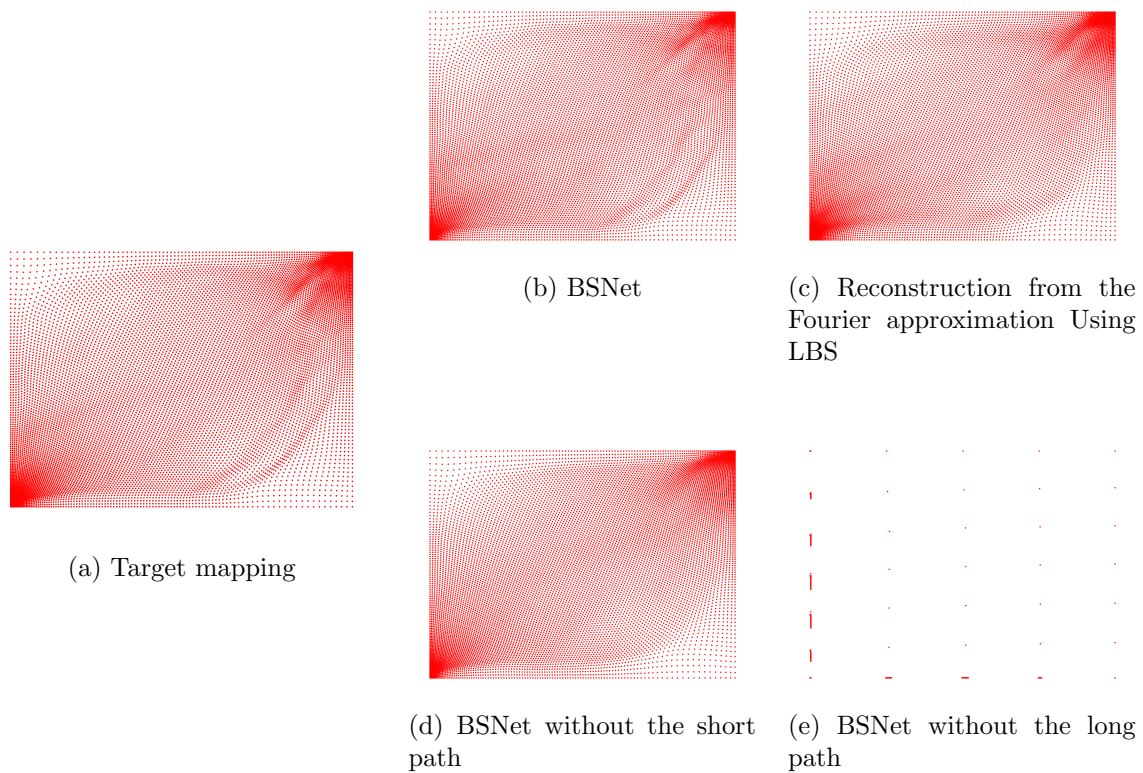


Figure 11: Examples generated by experiment of removing the short path or the long path.

7.3. Underwater Image Registration. When capturing underwater images, it is common that the images are distorted. The inhomogeneity in different parts of the seawater caused by temperature, salinity, density and small particles leads to different refraction index so as to affect the transmission of light. In this case, image registration algorithms can help restore the distorted images according to some known correct images.

In the training stage, we generate image pairs for registration by deforming images in the training set of ILSVRC2012 using deformation mappings generated by LBS or BSNet with μ consisting of two 112×112 images acting as the real and imaginary parts with the same method mentioned in [subsection 4.1](#). Then Estimator accepts the image pairs as its input and outputs two-channel images representing the Beltrami coefficients and acting as the input of the BSNet. Optimizing the Estimator with the loss function [\(4.8\)](#), a trained Estimator is obtained.

Then we select some underwater images from the validation set of ILSVRC2012 and deform them in the same manner performed in the training scheme to get the image pairs. Then we use the trained QCRegNet and VoxelMorph to restore the distorted underwater images. Comparing the restored images of the two methods, we find some interesting phenomena which demonstrate the superiority of our proposed method.

Increasing the supreme norm of the Beltrami coefficient which is used to generate the distorted images, we obtain large distortion images. Experiments on such images are conducted. To make the description abbreviate, we refer to the number of triangular faces where $|J| \leq 0$ as N_J and the sum of the absolute value of $|J|$ less than or equal to 0 as S_J . The registered images in the case of large distortion are shown in [Figure 12-Figure 17](#), which demonstrate that QCRegNet can preserve the diffeomorphism.

In order to obtain the distribution of the absolute value of the determinant of $|J| \leq 0$, we randomly generate 10000 Beltrami coefficients and 10000 distorted images from the validation set of ILSVRC2012, and use these data and the two trained models to generate the mappings. By calculating the determinant of the Jacobian matrix at each face, we obtain the distribution of the absolute value of faces whose $|J|$ less than or equal to 0, as shown in [Figure 18](#).

In this test, 8783 folded faces were found in the mappings generated by QCRegNet, while 12109 were found in that generated by VoxelMorph. Since the absolute value of the determinant of the majority of faces were less than 500000, we ignore those 72 faces which serve as the tail when drawing the histogram.

[Figure 18](#) shows that the number of folded faces of mappings generated by VoxelMorph is greater than that generated by QCRegNet. And the absolute value of the determinant of VoxelMorph is much greater than that of our proposed QCRegNet, which indicates that VoxelMorph encountered severe folding in some registration tasks, while our proposed QCRegNet successfully preserved the bijectivity.

7.4. Medical Image Registration. Diagnoses in diseases such as heart, lung and abdomen diseases usually rely on the comparison between several MRI slices. Precise registration between such slices can help experts to analyze the relationship between tissues at different time so as to diagnose illnesses.

In order to verify the feasibility of applying our model to medical scenarios, we conducted an experiment on the ACDC dataset [\[3\]](#) containing data from 150 multi-equipments MRI

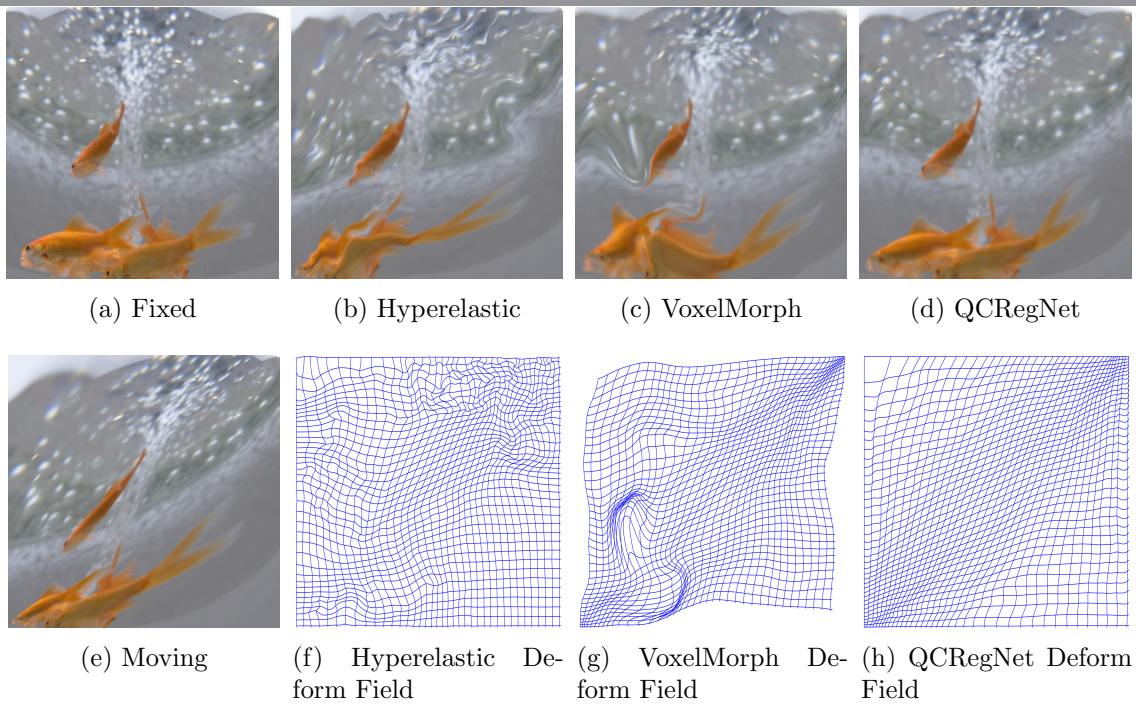


Figure 12: QCRegNet: $N_J = 0, S_J = 0$, VoxelMorph: $N_J = 58, S_J = 4727236.7533$

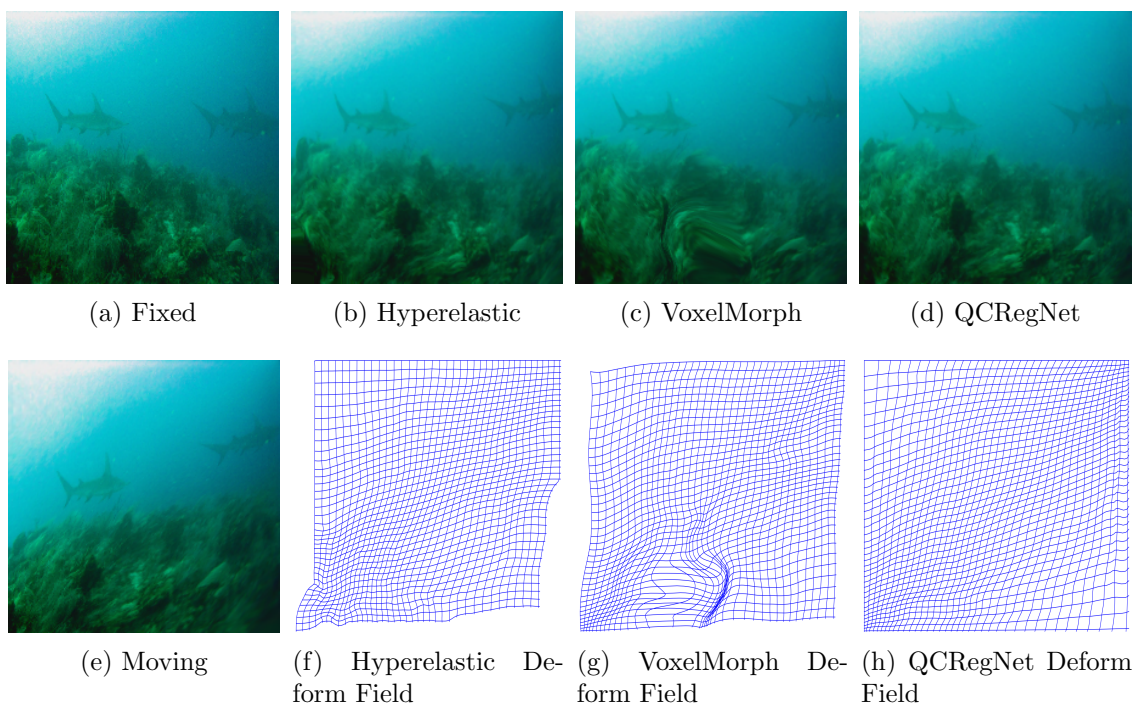


Figure 13: QCRegNet: $N_J = 0, S_J = 0$, VoxelMorph: $N_J = 2, S_J = 479.7763$

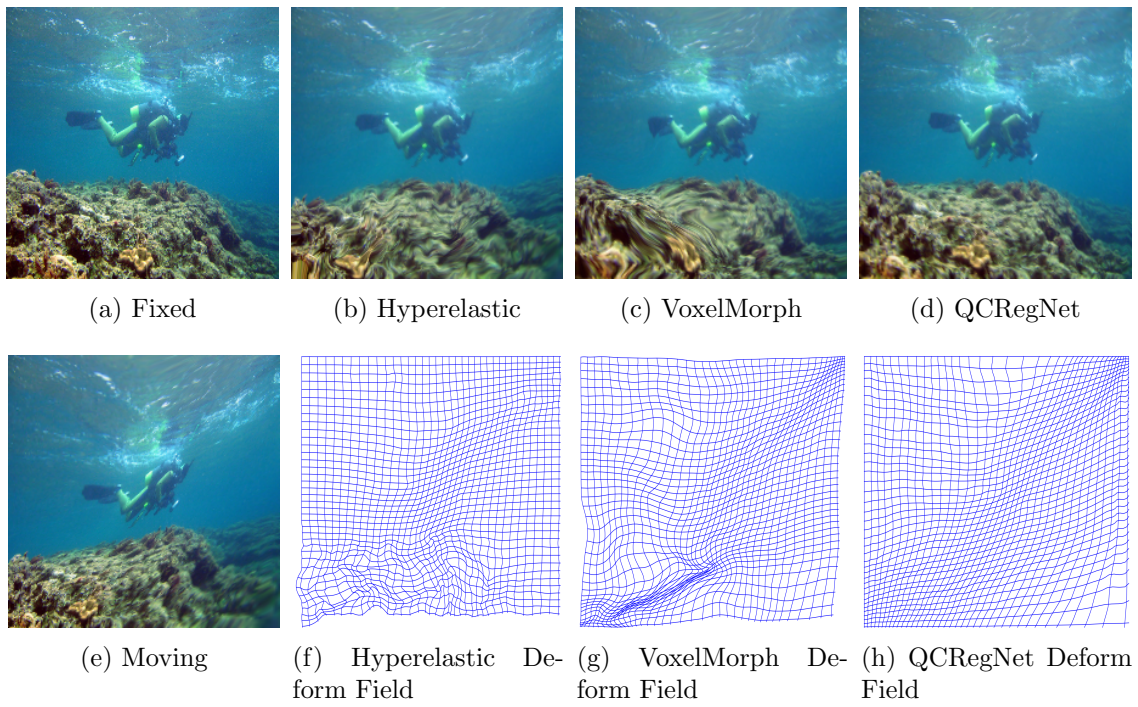


Figure 14: QCRegNet: $N_J = 0, S_J = 0$, VoxelMorph: $N_J = 186, S_J = 5693054.9218$

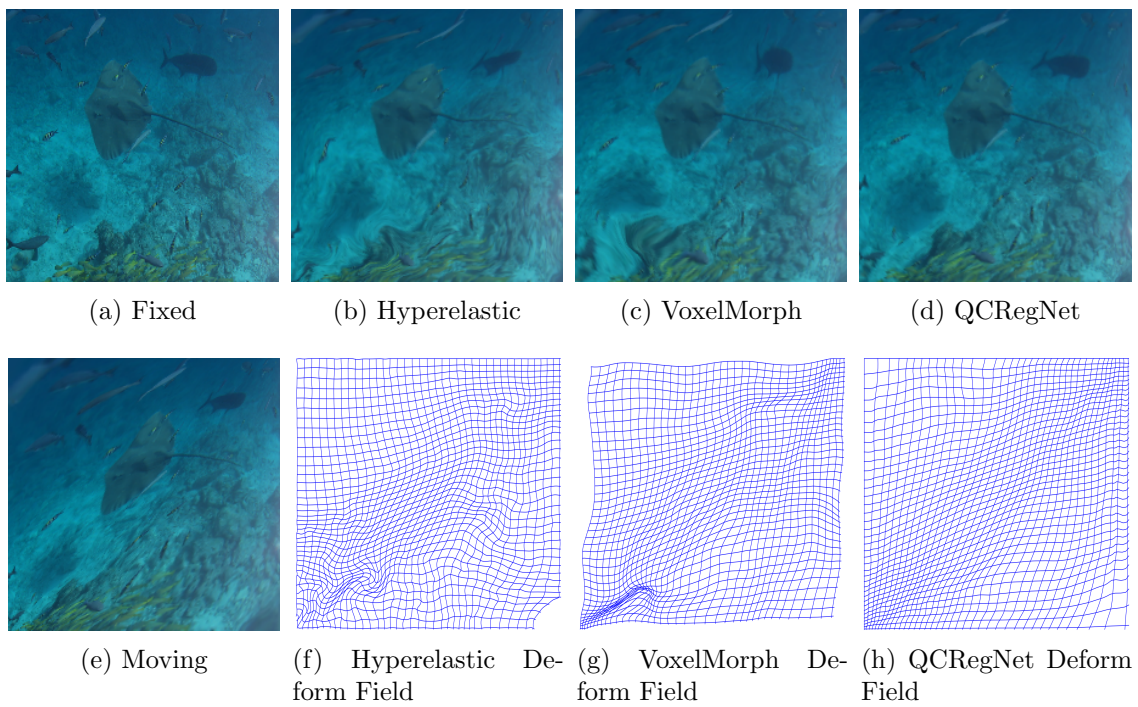


Figure 15: QCRegNet: $N_J = 0, S_J = 0$, VoxelMorph: $N_J = 3, S_J = 25612.5780$

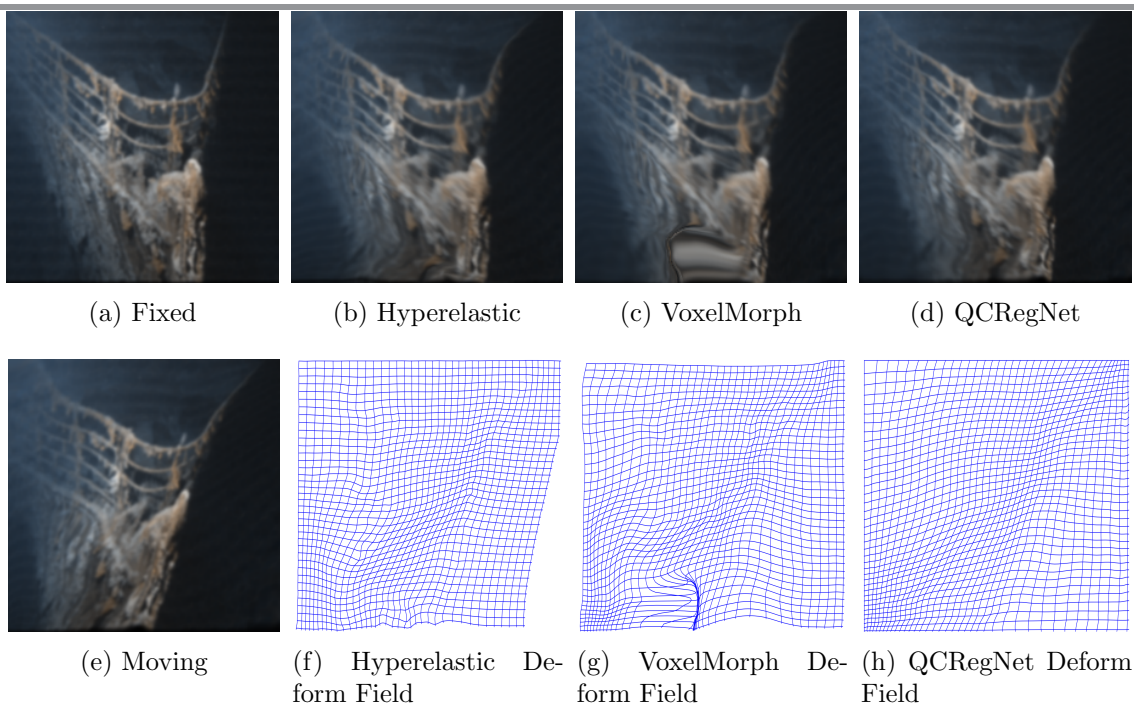


Figure 16: QCRegNet: $N_J = 0, S_J = 0$, VoxelMorph: $N_J = 20, S_J = 13066.9024$

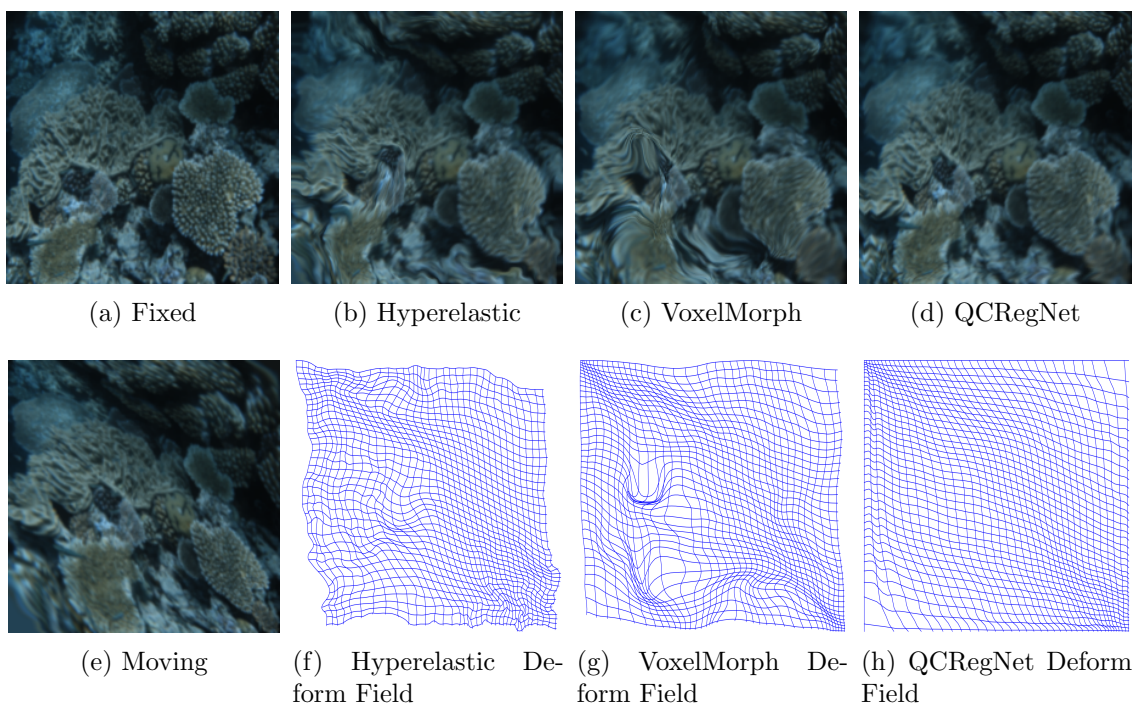
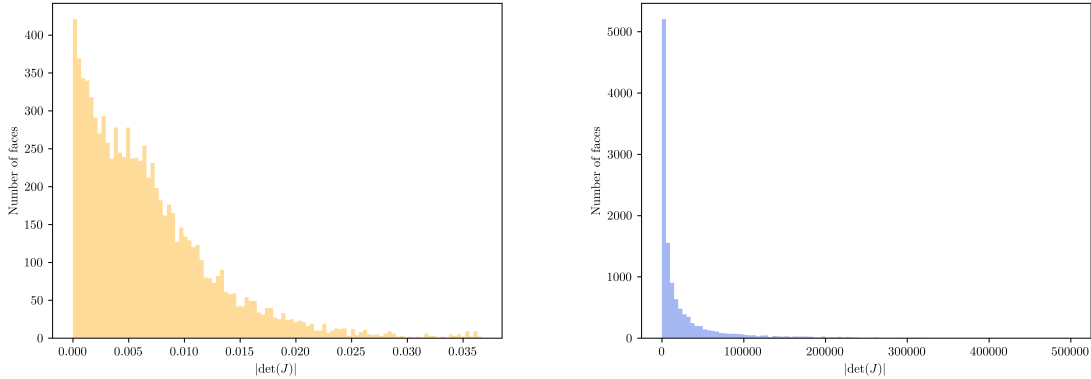


Figure 17: QCRegNet: $N_J = 0, S_J = 0$, VoxelMorph: $N_J = 7, S_J = 13042.7050$



(a) QCRegNet: 8783 folded faces, the mean absolute value is 0.0068, the maximal absolute value is 0.0367
 (b) VoxelMorph: 12109 folded faces, the mean absolute value is 33731.3366, the maximal absolute value is 1628854.0325. In this figure, the 72 faces, the tail of the histogram whose absolute values are greater than 500000, are not displayed.

Figure 18: Comparison of the distribution of the absolute value of faces whose $|J|$ less than or equal to 0. Notice that the scale on the horizontal axis in (b) is much larger than that in (a), which indicate that folding in the mappings generated by VoxelMorph is much more serious than that generated by QCRegNet.

recordings acquired from real clinical exams.

ACDC dataset includes a training set with 100 scans and a testing set with 50 scans. Each scan records a patient’s heartbeat, including the diastolic and systolic phases. In our experiment, we use the training set for training and the testing set for validation. Instead of using the data directly, we perform some data augmentation to obtain more data to train our model.

Firstly, splitting the samples along the shortest axis, we get a frontal view of the scan at different depths. Then we randomly select two scans from the same patient at the same depth. Due to the difference in the diastolic and systolic degrees at different times, the heart and peripheral tissue have different degrees of deformation. Then we randomly rotate the pair of samples and cut a pair of patches from the sample. Such a pair of patches serves as the input of our model.

The hyper-parameters settings are the same as that in [subsection 7.3](#). Some experimental results are shown in [subsection 7.4](#). Experimental results show that our proposed model can successfully handle the MRI registration. That MRI has large deformation implies that our model can be applied to real-world medical registration tasks.

8. Conclusion. Combining the Quasi-conformal theory and convolutional neural network, we introduce Quasi-conformal Registration Network (QCRegNet). QCRegNet takes the advantage of Quasi-conformal mapping to preserve the diffeomorphism of the mapping between

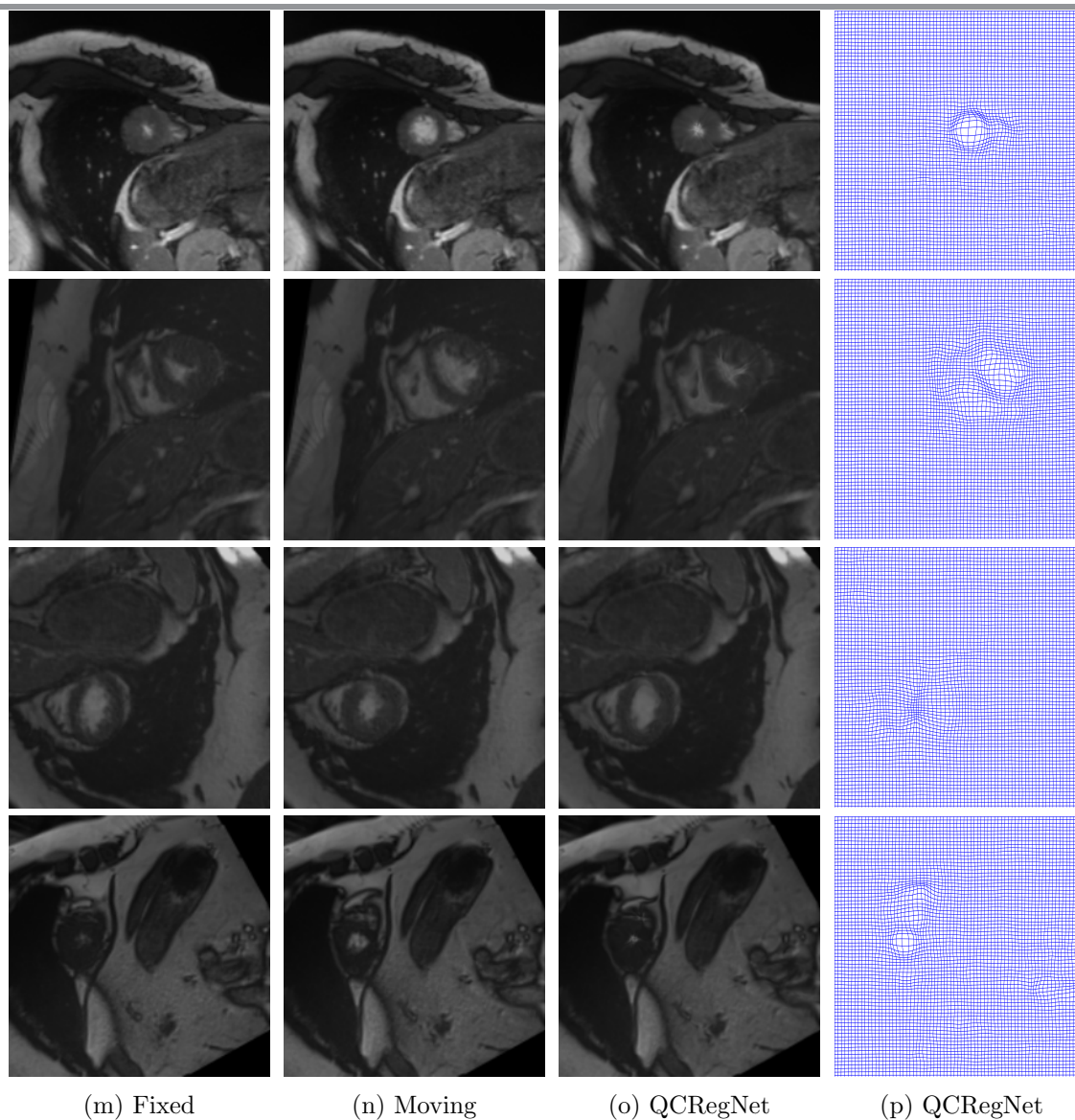


Figure 19: Results in medical registration

the fixed and moving images, and utilize the convolution operation to extract the distortion information from the images. We also propose the domain transform layer which makes it possible to use compressed Beltrami representation to represent the global distortion information. Experiments has been carried out to demonstrate the superiority of our model in preserving the topological information even when the distortion is very large, and showing good registration performance at the same time.

REFERENCES

- [1] G. BALAKRISHNAN, A. ZHAO, M. R. SABUNCU, J. GUTTAG, AND A. V. DALCA, *Voxelmorph: a learning framework for deformable medical image registration*, IEEE transactions on medical imaging, 38 (2019), pp. 1788–1800.
- [2] M. F. BEG, M. I. MILLER, A. TROUVÉ, AND L. YOUNES, *Computing large deformation metric mappings via geodesic flows of diffeomorphisms*, International journal of computer vision, 61 (2005), pp. 139–157.
- [3] O. BERNARD, A. LALANDE, C. ZOTTI, F. CERVENANSKY, X. YANG, P.-A. HENG, I. CETIN, K. LEKADIR, O. CAMARA, M. A. G. BALLESTER, ET AL., *Deep learning techniques for automatic mri cardiac multi-structures segmentation and diagnosis: is the problem solved?*, IEEE transactions on medical imaging, 37 (2018), pp. 2514–2525.
- [4] M. BURGER, J. MODERSITZKI, AND L. RUTHOTTO, *A hyperelastic regularization energy for image registration*, SIAM Journal on Scientific Computing, 35 (2013), pp. B132–B148.
- [5] G. P. CHOI, D. QIU, AND L. M. LUI, *Shape analysis via inconsistent surface registration*, Proceedings of the Royal Society A, 476 (2020), p. 20200147.
- [6] B. D. DE VOS, F. F. BERENDSEN, M. A. VIERGEVER, H. SOKOOTI, M. STARING, AND I. IŞGUM, *A deep learning framework for unsupervised affine and deformable image registration*, Medical image analysis, 52 (2019), pp. 128–143.
- [7] F. GARDINER, N. LAKIC, AND A. M. SOCIETY, *Quasiconformal Teichmüller Theory*, Mathematical surveys and monographs, American Mathematical Society, 2000, <https://books.google.com/books?id=BLfyBwAAQBAJ>.
- [8] B. GLOCKER, A. SOTIRAS, N. KOMODAKIS, AND N. PARAGIOS, *Deformable medical image registration: setting the state of the art with discrete methods*, Annual review of biomedical engineering, 13 (2011), pp. 219–244.
- [9] I. GOODFELLOW, Y. BENGIO, AND A. COURVILLE, *Deep Learning*, MIT Press, 2016. <http://www.deeplearningbook.org>.
- [10] B. K. HORN AND B. G. SCHUNCK, *Determining optical flow*, Artificial intelligence, 17 (1981), pp. 185–203.
- [11] M. JADERBERG, K. SIMONYAN, A. ZISSERMAN, AND K. KAVUKCUOGLU, *Spatial transformer networks*, arXiv preprint arXiv:1506.02025, (2015).
- [12] S. C. JOSHI AND M. I. MILLER, *Landmark matching via large deformation diffeomorphisms*, IEEE transactions on image processing, 9 (2000), pp. 1357–1370.
- [13] S. KLEIN, M. STARING, K. MURPHY, M. A. VIERGEVER, AND J. P. PLUIM, *Elastix: a toolbox for intensity-based medical image registration*, IEEE transactions on medical imaging, 29 (2009), pp. 196–205.
- [14] K. C. LAM AND L. M. LUI, *Landmark-and intensity-based registration with large deformations via quasi-conformal maps*, SIAM Journal on Imaging Sciences, 7 (2014), pp. 2364–2392.
- [15] L. M. LUI, K. C. LAM, T. W. WONG, AND X. GU, *Texture map and video compression using beltrami representation*, SIAM Journal on Imaging Sciences, 6 (2013), pp. 1880–1902.
- [16] J. MODERSITZKI, *FAIR: flexible algorithms for image registration*, SIAM, 2009.
- [17] A. PASZKE, S. GROSS, F. MASSA, A. LERER, J. BRADBURY, G. CHANAN, T. KILLEEN, Z. LIN, N. GIMELSHEIN, L. ANTIGA, A. DESMAISON, A. KOPF, E. YANG, Z. DEVITO, M. RAISON, A. TEJANI, S. CHILAMKURTHY, B. STEINER, L. FANG, J. BAI, AND S. CHINTALA, *Pytorch: An imperative style, high-performance deep learning library*, in Advances in Neural Information Processing Systems 32, H. Wallach, H. Larochelle, A. Beygelzimer, F. d'Alché-Buc, E. Fox, and R. Garnett, eds., Curran Associates, Inc., 2019, pp. 8024–8035, <http://papers.neurips.cc/paper/9015-pytorch-an-imperative-style-high-performance-deep-learning-library.pdf>.
- [18] O. RONNEBERGER, P. FISCHER, AND T. BROX, *U-net: Convolutional networks for biomedical image segmentation*, in Medical Image Computing and Computer-Assisted Intervention – MICCAI 2015, N. Navab, J. Hornegger, W. M. Wells, and A. F. Frangi, eds., Cham, 2015, Springer International Publishing, pp. 234–241.
- [19] O. RUSSAKOVSKY, J. DENG, H. SU, J. KRAUSE, S. SATHEESH, S. MA, Z. HUANG, A. KARPATY, A. KHOSLA, M. BERNSTEIN, A. C. BERG, AND L. FEI-FEI, *ImageNet Large Scale Visual Recognition Challenge*, International Journal of Computer Vision (IJCV), 115 (2015), pp. 211–252, <https://doi.org/10.1007/s11264-015-0699-4>.

- [org/10.1007/s11263-015-0816-y](https://doi.org/10.1007/s11263-015-0816-y).
- [20] J.-P. THIRION, *Image matching as a diffusion process: an analogy with maxwell's demons*, Medical image analysis, 2 (1998), pp. 243–260.
 - [21] T. VERCAUTEREN, X. PENNEC, A. PERCHANT, AND N. AYACHE, *Diffeomorphic demons: Efficient non-parametric image registration*, NeuroImage, 45 (2009), pp. S61–S72.
 - [22] C. P. YUNG, G. P. CHOI, K. CHEN, AND L. M. LUI, *Efficient feature-based image registration by mapping sparsified surfaces*, Journal of Visual Communication and Image Representation, 55 (2018), pp. 561–571.